iScience

CellPress
OPEN ACCESS

Article

Oxygen vacancy enhanced photocatalytic activity of Cu_2O/TiO_2 heterojunction

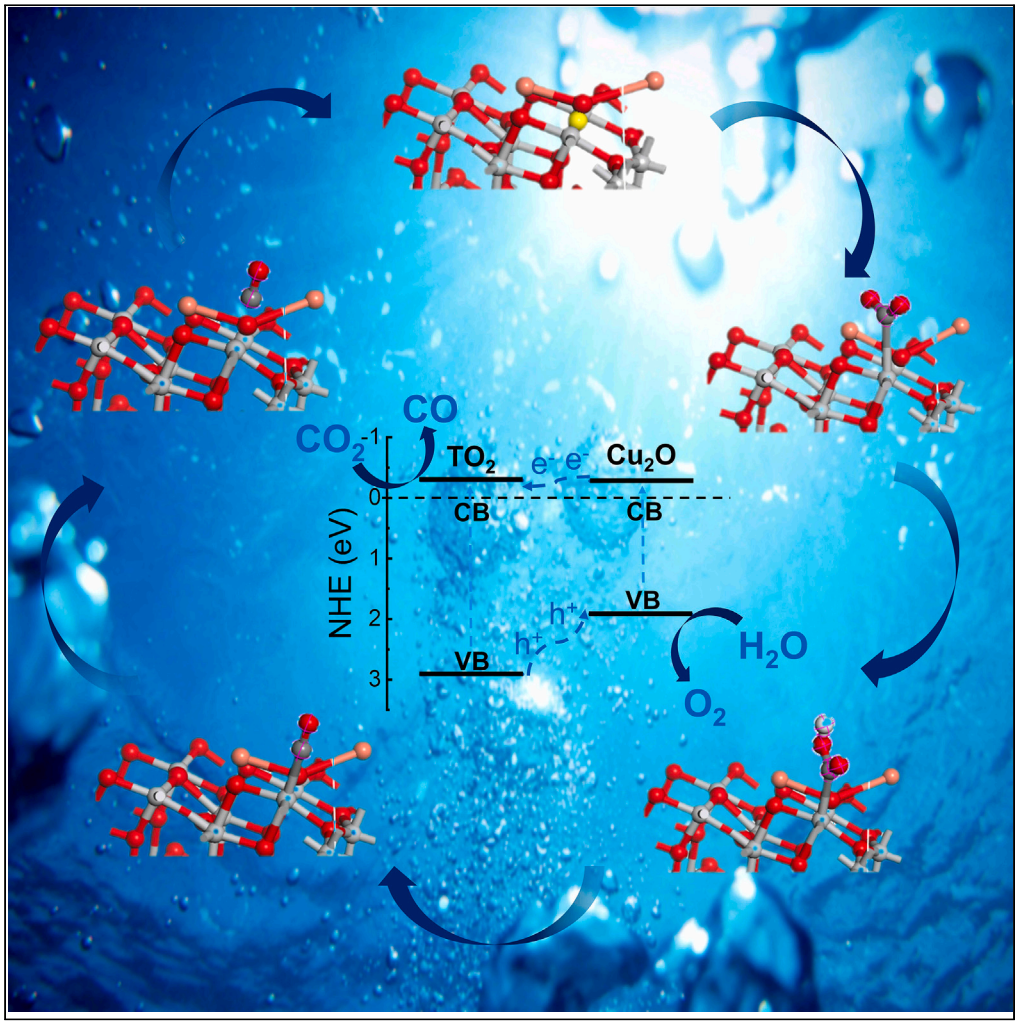

Hong Qian, Binxia Yuan, Yuhao Liu, Rui Zhu, Weiling Luan, Chengxi Zhang

yuanbinxia100@163.com (B.Y.)
luan@ecust.edu.cn (W.L.)

Highlights

The Cu_2O/TiO_2 heterojunction with oxygen vacancy is obtained by one-step method

The CO yield of Cu_2O/TiO_2 is 1.85 times that of TiO_2, with 10.22 μmol g^{-1} h^{-1}

The performance is the best when the mass fraction of Cu is between 0.075%–0.55%

The free energy of Cu_2O/TiO_{2O_v} from $*CO_2$ to *COOH is 0.088 eV lower than that of TiO_2

Qian et al., iScience 27, 109578
May 17, 2024
https://doi.org/10.1016/j.isci.2024.109578

iScience

CellPress
OPEN ACCESS

Article

Oxygen vacancy enhanced photocatalytic activity of Cu_2O/TiO_2 heterojunction

Hong Qian,[1] Binxia Yuan,[1,2,4,*] Yuhao Liu,[1] Rui Zhu,[1] Weiling Luan,[2,*] and Chengxi Zhang[3]

SUMMARY

In this study, a method was developed to create oxygen vacancies in Cu_2O/TiO_2 heterojunctions. By varying the amounts of ethylenediaminetetraacetic acid (EDTA), sodium citrate, and copper acetate, Cu_2O/TiO_2 with different Cu ratios were synthesized. Tests on CO_2 photocatalytic reduction revealed that Cu_2O/TiO_2's performance is influenced by Cu content. The ideal Cu mass fraction in Cu_2O/TiO_2, determined by inductively coupled plasma (ICP), is between 0.075% and 0.55%, with the highest CO yield being 10.22 $\mu mol\ g^{-1}\ h^{-1}$, significantly surpassing pure TiO_2. High-resolution transmission electron microscopy and electron paramagnetic resonance studies showed optimal oxygen vacancy in the most effective heterojunction. Density functional theory (DFT) calculations indicated a 0.088 eV lower energy barrier for $*CO_2$ to *COOH conversion in Cu_2O/TiO_2 with oxygen vacancy compared to TiO_2, suggesting that oxygen vacancies enhance photocatalytic activity.

INTRODUCTION

TiO_2 is one of the most widely studied semiconductors for environmental and energy issues.[1–3]- However, the photocatalytic efficiency of TiO_2 is limited by its wide bandgap and high recombination rate of photo-generated charge carriers. The use of narrow bandgap semiconductor Cu_2O modification to construct heterojunctions has also attracted widespread attention.[4,5]

In theory, the difference in band structure between TiO_2 and Cu_2O can easily lead to the formation of type II heterojunctions,[6] S-type heterojunctions,[7] and Z-type heterojunctions.[8] However, TiO_2 and Cu_2O may not form heterostructures during preparation, or the resulting heterostructures may not significantly improve catalytic activity.[9] The catalytic performance of heterojunction materials is related to the morphology, interfacial contact, dispersibility, and oxygen vacancy defects.[10–13] Among them, the heterojunction with strong interface contact is helpful to electron transfer, and the oxygen vacancies can also provide more active sites for CO_2 adsorption. Xue et al.[14] prepared a p-type Cu_2O nanoparticle-coated n-type TiO_2 nanotube (TNTs) array-based coaxial heterostructure using a combination of anodization and electrodeposition methods. It was found that the ribs formed during anodization and the added thiourea during electrodeposition played a crucial role in forming the Cu_2O nanoparticle heterostructure. Bai et al.[15] fabricated a uniform p-Cu_2O/n-TiO_2 heterojunction electrode using electrochemical anodization and pulse electrodeposition methods, which exhibited enhanced photoelectrocatalytic (PEC) activity for the degradation of chloramphenicol. Wei et al.[16] stabilized Cu_2O by adjusting the exposed surfaces and structural defects of TiO_2, showing that oxygen vacancy defects enhanced charge separation and effective removal of oxidized holes of Cu_2O. However, the fabrication methods for Cu_2O/TiO_2 heterojunctions are complex and not conducive to large-scale production. Although small-sized samples increase surface area, they are more prone to aggregation, thereby reducing catalytic performance.[17] Meanwhile, excessive bulk oxygen vacancies can also create electron traps,[18] which are detrimental to catalytic reactions. Therefore, controlling the ratio of surface oxygen vacancies to bulk oxygen vacancies is crucial for improving performance.

This work uses a simple one-step hydrothermal method to prepare Cu_2O/TiO_2 heterojunction photocatalytic materials with strong interface contact, high dispersion, and oxygen vacancies. The experimental results indicate that an appropriate amount of Cu^{2+} is beneficial for improving photocatalytic properties, and the photocatalytic reaction mechanism of Cu_2O/TiO_2 with oxygen vacancies has been calculated using density functional theory (DFT).

RESULTS AND DISCUSSION

The influences of EDTA, sodium citrate, and copper acetate on the composition of samples are investigated. Generally, the XRD diffraction peak of Cu_2O gradually increases with the increase of copper acetate. Comparing Figures 1A and S1A, it can be observed that as the amount of EDTA increases, the XRD diffraction peak of Cu_2O decreases, while the diffraction peak of TiO_2 remains unchanged. Comparing Figures 1A and S1B, it can be seen that as the amount of sodium citrate increases, the diffraction peak of Cu_2O becomes more pronounced, while the

[1]College of Energy and Mechanical Engineering, Shanghai University of Electric Power, Shanghai 201306, P.R. China
[2]School of Mechanical and Power Engineering, East China University of Science and Technology, Shanghai 200237, China
[3]Department of Optoelectronic Information Science and Engineering, School of Science, Jiangsu University of Science and Technology, Zhenjiang 212100, China
[4]Lead contact
*Correspondence: yuanbinxia100@163.com (B.Y.), luan@ecust.edu.cn (W.L.)
https://doi.org/10.1016/j.isci.2024.109578

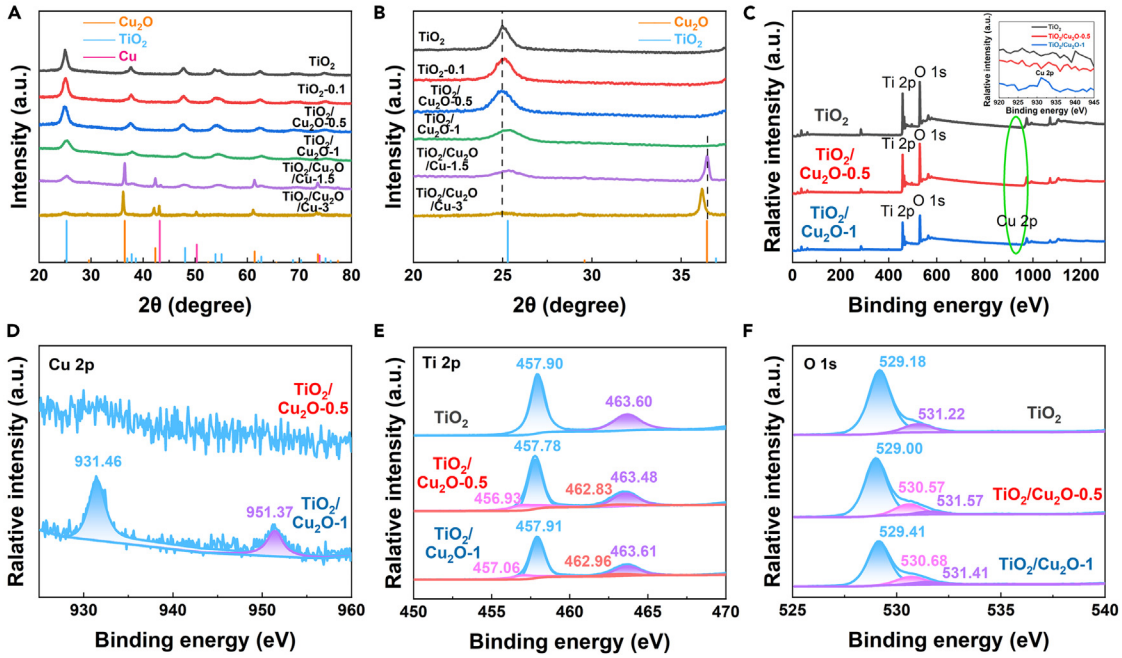

Figure 1. The samples obtained at the different amounts of $Cu(OAc)_2$ under the conditions of 1 mmol EDTA and 0.3 mmol sodium citrate

(A and B) XRD patterns; XPS spectra.

(C) Survey.

(D) Cu2p.

(E) Ti2p, and (F) O1s.

diffraction peak of TiO_2 is significantly affected. It indicates that EDTA and sodium citrate are essential in generating Cu_2O and TiO_2, respectively.

Figures 1A and 1B show the XRD patterns of samples obtained by different copper acetate contents under 1 mmol EDTA and 0.3 mmol sodium citrate. When the molar amount of $Cu(OAc)_2$ is less than or equal to 1 mmol, only the diffraction peak of anatase TiO_2 (PDF # 21–1272) can be seen. It can be seen from the TiO_2/Cu_2O-1 sample that there is a significant right shift in the TiO_2 (101) crystal plane, indicating the presence of lattice defects in TiO_2. When the molar amount of $Cu(OAc)_2$ is greater than 1.5 mmol, the Cu_2O (PDF # 78–2076) diffraction and Cu diffraction peaks are detected, indicating $Cu_2O/TiO_2/Cu$ composite material.

Through X-ray photoelectron spectroscopy (XPS) testing, it is found that there are characteristic peaks of Cu2p orbitals in the TiO_2/Cu_2O-1 sample (Figure 1C). After fitting the XPS spectra of the Cu2p orbitals (Figure 1D), the characteristic peaks at 931.46 eV and 951.37 eV correspond to Cu^+, indicating the presence of Cu_2O. Although the characteristic peak of the $Cu2p_{3/2}$ orbitals near 931.5 eV in the TiO_2/Cu_2O-0.5 sample is not significant, a trending peak can still be observed. The Ti 2p peak in TiO_2/Cu_2O-0.5 has an asymmetric shape, with four peaks at 456.93 eV, 462.83 eV, 457.78 eV, and 463.48 eV, corresponding to Ti^{3+} $2p_{3/2}$, Ti^{3+} $2p_{1/2}$, Ti^{4+} $2p_{3/2}$, and Ti^{4+} $2p_{1/2}$, respectively.[19] Based on the peak area calculations, the ratio of Ti^{3+}/Ti^{4+} in TiO_2/Cu_2O-0.5 and TiO_2/Cu_2O-1 is approximately 27% and 21%, respectively. Thus, TiO_2/Cu_2O-0.5 exhibits more surface oxygen vacancies compared to TiO_2/Cu_2O-1.[20] The peaks at 529.00 eV, 530.57 eV, and 531.57 eV in the O1s orbital correspond to lattice oxygen (Cu_2O and TiO_2), oxygen vacancies, and hydroxyl groups adsorbed on the catalyst surface, respectively.[21–23] In addition, oxygen vacancies can enhance the catalyst's adsorption capacity for hydroxyl and H_2O molecules, thereby increasing the adsorption of H^+ and enhancing catalytic performance in CO_2 reduction reactions.

From Figure 2A, the anatase TiO_2 obtained without $Cu(OAc)_2$ exhibits a mixture of rhombic and small particles. When the copper acetate is added, the large rhombic TiO_2 is decomposed into small particles. When the amount of copper acetate is 0.1–1 mmol, the sample has uniform morphology and high dispersibility, see Figures 2B–2D. In the high resolution transmission electron microscope (HRTEM) image of the TiO_2/Cu_2O sample (Figure 2G), we detected that lattice spacings of 0.242 nm and 0.353 nm correspond to the Cu_2O (111) and TiO_2 (101) crystal planes, respectively. Furthermore, significant oxygen vacancies are observed in both TiO_2 and Cu_2O, particularly with noticeable lattice distortions near the interface of TiO_2 and Cu_2O (Figure S6). Lattice distortions can result in displacements and distortions of atomic positions, causing local strains and distortions. The distortions can lead to changes in the positions of nearby oxygen atoms, creating vacancies or defects in the vicinity, thereby forming oxygen vacancies. Meantime, the formation of oxygen vacancies may also induce lattice distortions. When oxygen atoms depart from their original positions in the lattice, surrounding atoms may readjust to maintain overall balance and stability, leading to lattice distortions. Comparing the TEM images of different EDTA and sodium citrate samples (Figure S2), when the amount of copper acetate used is small, increasing sodium citrate or reducing EDTA will cause the development of the sample toward a sheet-like structure. When the amount of copper acetate is high, sodium citrate and EDTA have little effect on the sample's morphology, mainly consisting of

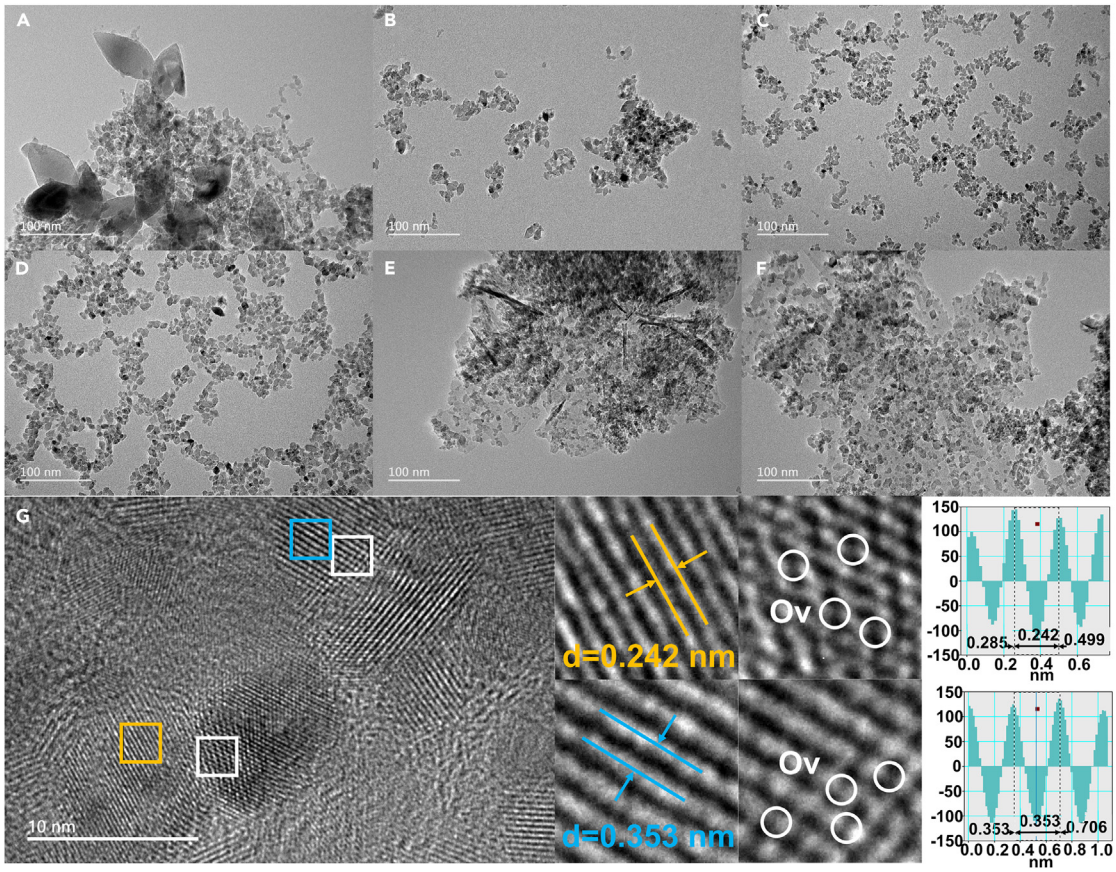

Figure 2. TEM images of different sample

(A) TiO_2.

(B) TiO_2-0.1.

(C) TiO_2/Cu_2O-0.5.

(D) TiO_2/Cu_2O-1.

(E) TiO_2/Cu_2O/Cu-1.5.

(F) TiO_2/Cu_2O/Cu-3.

(G) HRTEM images of TiO_2/Cu_2O-1.

small particles. It is consistent with the conclusion obtained by XRD that EDTA and sodium citrate affect the generation of Cu_2O and TiO_2, respectively.

Figures 3A and 3B show the CO yield of CO_2 reduction in all samples. As the amount of copper acetate increases, the average CO yield decreases. When the amounts of copper acetate are 0.5 mmol and 1 mmol, the yields of CO are 10.22 μmol g^{-1} h^{-1} and 9.41 μmol g^{-1} h^{-1}, which are 1.85 times and 1.70 times that of the sample without copper acetate. The results indicate that the formation of Cu_2O/TiO_2 heterojunction significantly improves the catalytic performance of TiO_2. To further confirm the stability of the catalytic performance of the heterojunction catalyst, the cyclic photocatalytic tests are conducted on the TiO_2/Cu_2O-0.5 sample, as shown in Figure 3D. After 3 cycles, the CO production remains at the same level, indicating the excellent photocatalytic stability. Compared to other heterojunctions reported in the literature, the TiO_2/Cu_2O-0.5 sample prepared in our work exhibits excellent catalytic activity (Figure 3E).[8,24–34] When the amounts of copper acetate are 1.5 mmol and 3 mmol, the yields of CO are 7.91 μmol g^{-1} h^{-1} and 5.7 μmol g^{-1} h^{-1}, respectively. The increase of Cu and the decrease of TiO_2 is not conducive to CO_2 conversion. In the meantime, the contents of Cu element in TiO_2/Cu_2O-0.1, TiO_2/Cu_2O-0.5, and TiO_2/Cu_2O-1 samples are determined by inductively coupled plasma technology (ICP). Thus, when the Cu element content in the sample is between 0.075% and 0.5501%, the catalytic activity of the Cu_2O/TiO_2 heterojunction catalyst is the best. Excessive proportion of Cu_2O in Cu_2O/TiO_2 system can affect its catalytic performance, see Figure S3.

To investigate the reasons for the improved CO_2 reduction performance of Cu_2O/TiO_2 photocatalysts, the instantaneous photocurrent response (i-t curve) is used to characterize the photo response ability (Figure 3F). It can be seen that there is no apparent photocurrent record in the dark and the photocurrent of all samples increases at the moment of illumination. However, the TiO_2 sample shows a clear "shark peak" after illumination. In contrast, the TiO_2/Cu_2O-0.5 sample shows a "rectangular peak", indicating that the photo-generated electrons and holes in the TiO_2/Cu_2O-0.5 sample can quickly reach the optimal separation state after illumination excitation, which is conducive to the rapid

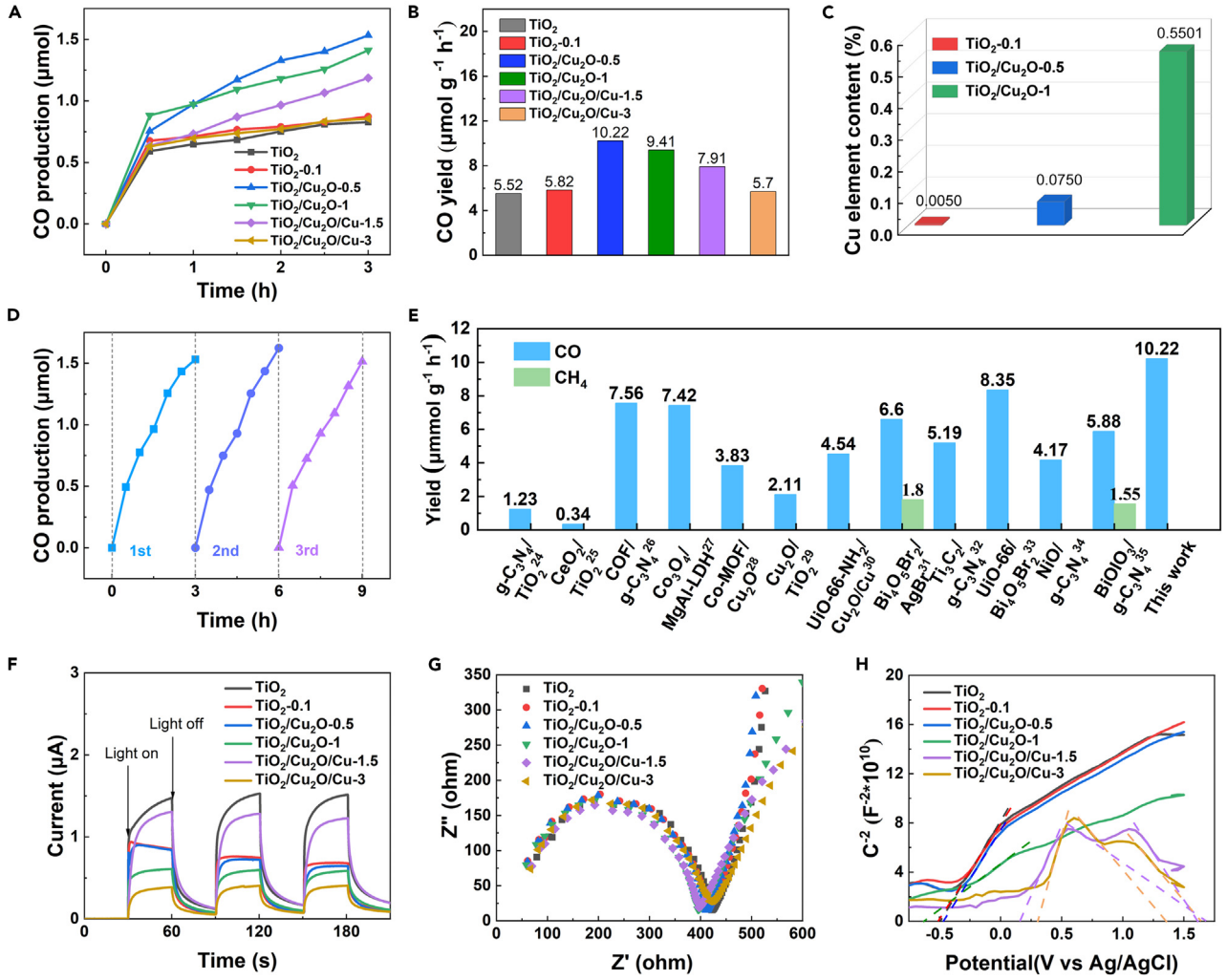

Figure 3. Photocatalysis and optoelectronic performance

(A) photocatalytic CO production.

(B) photocatalytic CO yield.

(C) ICP plot.

(D) TiO_2/Cu_2O-0.5 sample photocatalytic cycling test for CO production.

(E) Comparison chart of catalytic activity.

(F) I-t curve.

(G) EIS curve.

(H) M-S curve.

progress of catalytic reactions.[35] EIS is an effective technique for studying the interface resistance between semiconductors and electrolytes. In Figure 3G, the radii of all composite materials are smaller than that of the TiO_2 sample, indicating that the increase of Cu_2O reduces the resistance in the chemical reaction.

The Mott-Schottky (M-S) curve can be used to analyze the sample semiconductor material's type and carrier concentration. Figure 3H shows that as the amount of copper acetate increases, the curve exhibits positive and negative slopes, indicating the simultaneous presence of n-type (TiO_2) and p-type (Cu_2O) semiconductors in the composite material. Meanwhile, due to the low content of Cu_2O, the M-S curves of TiO_2-0.1, TiO_2/Cu_2O-0.5, and TiO_2/Cu_2O-1 samples are similar to that of the TiO_2 curve. The Mott-Schottky equation shows that the carrier concentration of a material is inversely proportional to the slope of the tangent line. The higher the carrier concentration, the lower the slope of the tangent line. Figure 3F shows that the slope of TiO_2/Cu_2O-1 is the smallest, indicating that the carrier concentration and electron migration rate in the TiO_2/Cu_2O-1 sample are the best.

When a small amount of copper acetate is added, the UV-visible spectra of the samples and the corresponding band gaps remain almost unchanged (Figure 4A). However, as the amount of copper acetate increases to 1.5 mmol and 3 mmol, the light response intensity decreases significantly, as shown in Figure S4. However, there is no significant difference in the band gap width, which is mainly because the content of

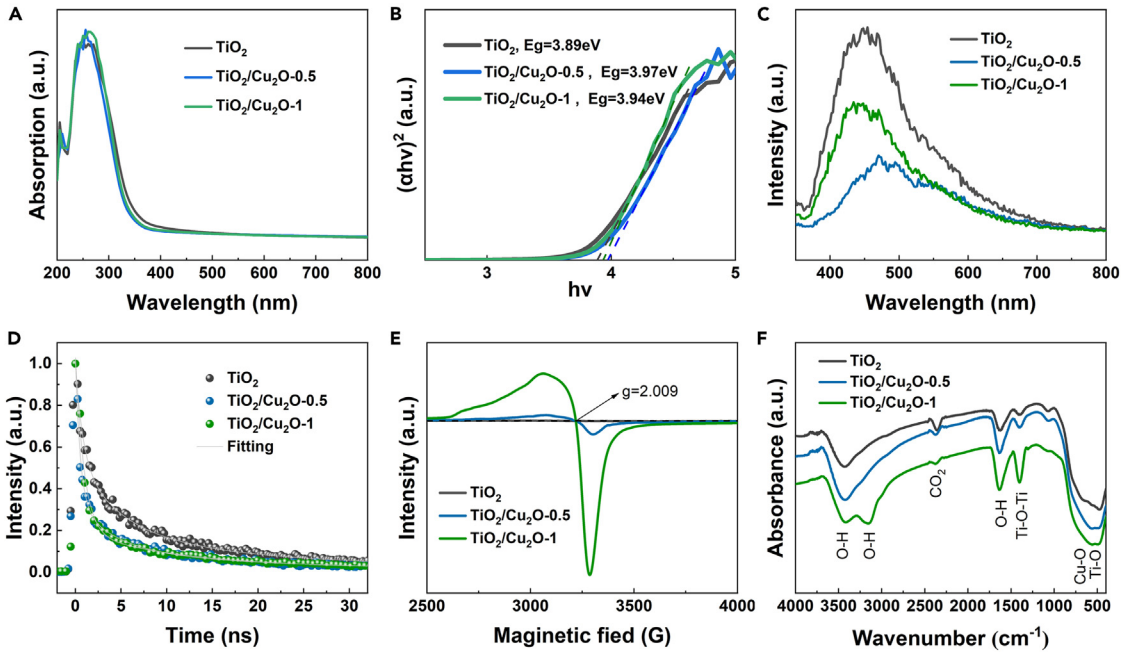

Figure 4. Optical performance and EPR measurement

(A) UV-vis absorption spectra.

(B) Band gap conversion spectra.

(C) PL.

(D) TRPL.

(E) EPR, and (F) FTIR.

Cu is very low. Photoluminescence (PL) spectroscopy evaluates the separation efficiency of photo-generated electrons and holes. As shown in Figure 4C, TiO_2/Cu_2O-0.5 exhibits the weakest PL signal, indicating the slowest electron-hole recombination rate. In addition, the dynamics of photo-generated carriers are further studied using TRPL measurements. Through fitting the corresponding TRPL curve with a third-order exponent, the average lifetime of TiO_2, TiO_2/Cu_2O-0.5, and TiO_2/Cu_2O-1 is 6.53 ns, 3.77 ns, and 3.91 ns, respectively (Table S1). Therefore, the average PL lifetime decay of heterojunction composite materials accelerates, indicating that Cu_2O/TiO_2 heterojunction formation accelerates interface charge transfer [16].

Electron paramagnetic resonance (EPR) measurement is the most potent characterization to confirm the presence of oxygen vacancies, as shown in Figure 4E. There is no signal of oxygen vacancies in the TiO_2 sample. As the amount of Cu^+ increases, the signal of oxygen vacancies gradually strengthens, indicating that the Cu_2O/TiO_2 heterojunction increases the number of oxygen vacancies in the composite material. The signal of TiO_2/Cu_2O-1 sample is significantly higher than that of TiO_2/Cu_2O-0.5 sample, indicating the presence of a large number of bulk oxygen vacancies.[36] Surface oxygen vacancies can enhance the separation of photo-generated electrons and holes, thereby improving catalytic activity. However, an excess of bulk oxygen vacancies can form electron traps, leading to increased recombination centers for photo-generated electrons and holes, thus inhibiting the participation of electrons in catalytic reduction reactions and reducing catalytic activity. It is consistent with the analysis from XPS and catalytic activity tests.

Fourier transform infrared spectroscopy (FTIR) has been used to study lattice vibrations. The peaks near 3,421 cm^{-1} and 3,150 cm^{-1} correspond to the O-H stretching vibration of hydroxyl groups and the O-H stretching vibration of hydrogen bonds, respectively. The peak at 2,365 cm^{-1} confirms the presence of CO_2 molecules measured in the air. 1,636 cm^{-1} belongs to the H-O-H bending vibration of water molecules physically adsorbed on the sample surface.[23] The peak near 1,400cm^{-1} corresponds to changes in the bond length of Ti-O-Ti and weaker Ti-OH bonding. The broadband in the 700–480 cm^{-1} region corresponds to anatase TiO_2, which belongs to Ti-O stretching and Ti-O-Ti bridging stretching.[37–39] Meanwhile, the stretching vibration of Cu-O also occurs around 500 cm^{-1}. Figure 4F shows that the O-H vibrational peaks in the TiO_2/Cu_2O-0.5 and TiO_2/Cu_2O-1 samples are more pronounced than the TiO_2 sample, exhibiting better water molecule adsorption capacity and providing more H^+ for CO_2 reduction. In addition, there is a significant enhancement of vibration peaks around 3,150 cm^{-1} and 1,400 cm^{-1} in the TiO_2/Cu_2O-1 sample, indicating that TiO_2 provides more oxygen vacancies for the co-absorption of water molecules and oxygen and forms hydrogen bonds. Meanwhile, there is a significant change in the frequency peak of Ti-O for 580 cm^{-1}, indicating the presence of more defects, especially oxygen vacancies. It confirms that the Cu_2O/TiO_2 heterojunction promotes the formation of TiO_2 oxygen vacancies and improves the hydrophilicity of the sample.

To further verify the mechanism of enhancing the catalytic activity of the heterojunction model, a perfect TiO_2 model and a Cu_2O/TiO_{2Ov} heterojunction model containing oxygen vacancies (Figure S5) are constructed by Materials Studio (MS) software. The catalytic properties are

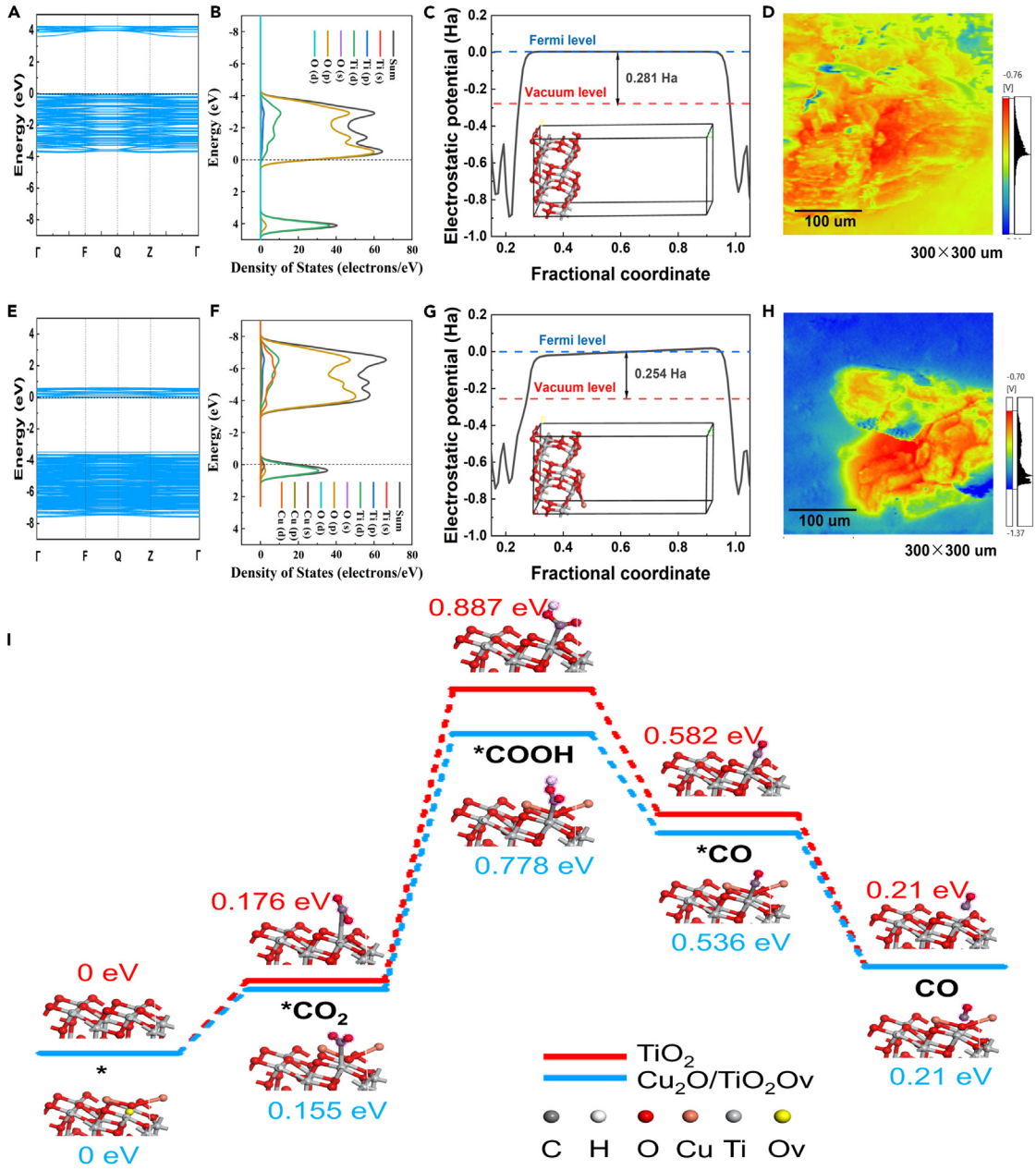

Figure 5. DFT theory

(A) Band energy of TiO_2.
(B) PDOS of TiO_2.
(C) Work function of TiO_2.
(D) SPM of TiO_2.
(E) Band energy of Cu_2O/TiO_{2Ov}.
(F) PDOS of Cu_2O/TiO_{2Ov}.
(G) Work function of Cu_2O/TiO_{2Ov}.
(H) SPM of TiO_2/Cu_2O-1.
(I) Free energy step diagrams of TiO_2 and Cu_2O/TiO_{2Ov}.

calculated using the DMol3 module. The energy band and density of states effectively reflect the occupied state and density of electrons at the Fermi level. With the emergence of oxygen vacancies and the recombination of Cu_2O, the energy band of the Cu_2O/TiO_{2Ov} model significantly shifts toward the valence band, indicating that the formation of heterostructures and oxygen vacancies has changed the original band edge position (Figures 5A and 5E). In addition to the original O2p orbitals, there are also electrons from Cu3d orbitals on the conduction band

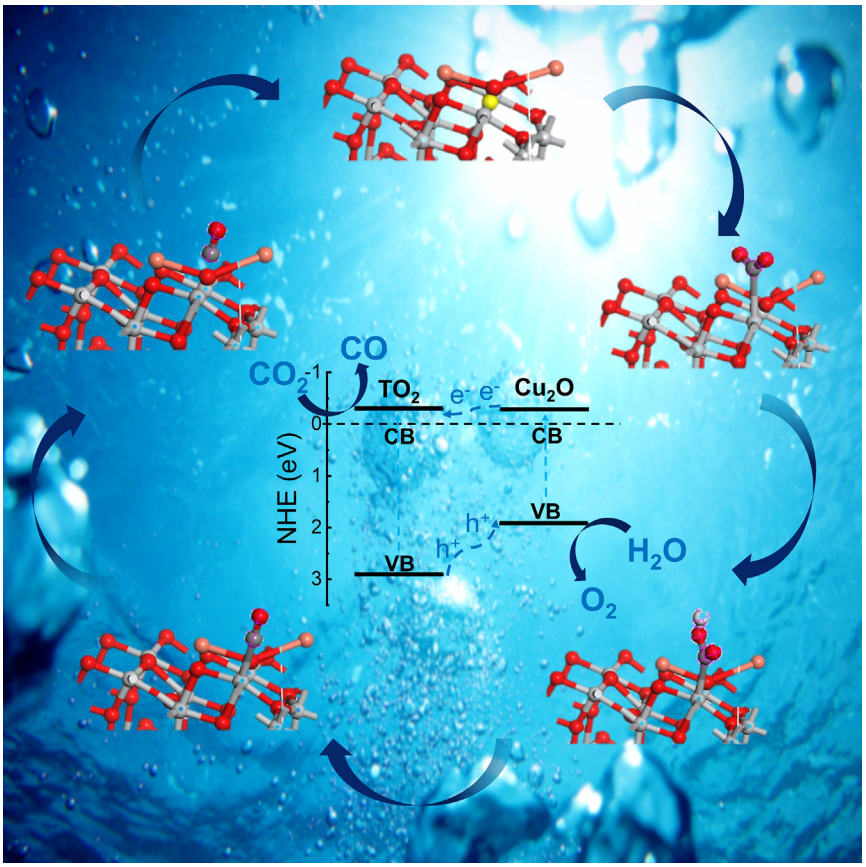

Figure 6. Reaction mechanism diagram

side, indicating that Cu_2O mainly affects the position of the conduction band and the electron distribution of O (Figures 5B and 5F). From Figures 5C and 5G, the work function of Cu_2O/TiO_{2Ov} (0.254 Ha) is smaller than that of perfect TiO_2 (0.281 Ha), indicating that Cu_2O/TiO_{2Ov} is more likely to become an electron acceptor. Cu_2O/TiO_{2Ov} has more electrons and a higher Fermi level, which is consistent with the changes in Fermi levels in energy bands and density of states. Meanwhile, the surface potentials of TiO_2 and TiO_2/Cu_2O-0.5 are measured using scanning probe microscopy (SPM) on a highly oriented pyrolytic graphite (HOPG) substrate, as shown in Figures 5D and 5H. The work function range obtained by selecting the electric potential with negative and positive potentials in the image through Equation 1,[40] is consistent with the calculated value by DFT. According to the free energy step diagram in Figure 5I, the free energy of the Cu_2O/TiO_{2Ov} sample decreased by 0.088 eV compared to the perfect TiO_2 in the $*CO_2$ to *COOH step, indicating that Cu_2O/TiO_{2Ov} has better catalytic performance.[41]

$$\Phi_{sample} = \Phi_{HOPG} + e^{\left(Test_{HOPG} - Test_{sample}\right)} \quad \text{(Equation 1)}$$

Based on the above experimental and theoretical results, the possible reaction mechanism is shown in Figure 6. When Cu_2O and TiO_2 are in close contact, electrons from the conduction band of Cu_2O transfer to the conduction band of TiO_2 for photocatalytic CO_2 reduction, while holes from the valence band of TiO_2 transfer to the valence band of Cu_2O for oxidation reactions, illustrating a typical Type II heterojunction.

To investigate the stability of the samples, XRD and TEM characterizations of the catalyst are performed before and after the catalytic reaction, as shown in Figure 7. The composition and morphology of the samples remain unchanged, indicating excellent stability of the heterojunction catalyst in terms of composition and morphology. Additionally, repeated preparations of the TiO_2/Cu_2O-0.5 sample are performed, and the samples are stored in ambient air at room temperature for 2 weeks and 4 weeks. The photocatalytic results show similar catalytic performances for the samples even after different storage times, demonstrating the good reproducibility of the catalyst preparation (Figure S7).

Conclusions

In summary, Cu_2O/TiO_2 heterojunction photocatalysts are prepared using a one-step method. Through adjusting the EDTA, sodium citrate, and copper acetate content, it can be found that EDTA and sodium citrate affect the composition and formation of Cu_2O and TiO_2. When the molar ratio of EDTA and sodium citrate is 1:0.3, the dispersion and photocatalytic performance of the sample are relatively good. When the

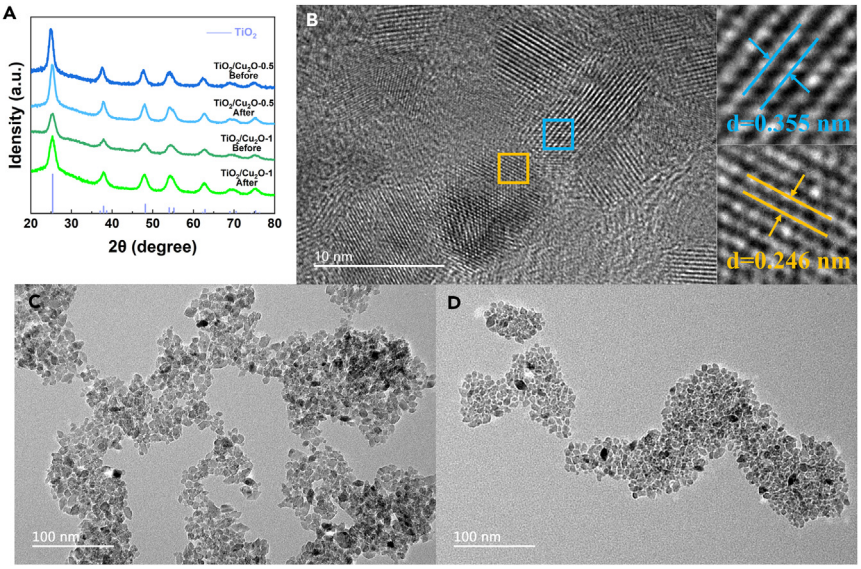

Figure 7. XRD and TEM before and after photocatalytic reaction

(A) XRD of samples TiO_2/Cu_2O-0.5 and TiO_2/Cu_2O-1 before and after photocatalytic reaction.

(B) HRTEM of TiO_2/Cu_2O-1 after photocatalytic reaction; TEM images after photocatalytic reaction.

(C) TiO_2/Cu_2O-0.5.

(D) TiO_2/Cu_2O-1.

copper acetate content is between 0.5 mmol and 1 mmol, ICP characterization reveals that the mass fraction of Cu element in Cu_2O/TiO_2 heterojunction is 0.075%–0.55%. The catalytic performance of TiO_2/Cu_2O-0.5 and TiO_2/Cu_2O-1 is better with 10.22 μmol g^{-1} h^{-1} and 9.41 μmol g^{-1} h^{-1}. XPS analysis confirms the presence of Cu_2O, Ti2p, and O1s orbitals in the 1 mmol copper acetate sample, indirectly confirming oxygen vacancies. In HRTEM, it is evident that the sample exhibits good dispersibility, lattice distortion, and oxygen vacancies. EPR characterization confirmed the presence of oxygen vacancies in the TiO_2/Cu_2O-0.5 and TiO_2/Cu_2O-1 samples. Compared with single TiO_2, the average fluorescence lifetimes of TiO_2/Cu_2O-0.5 and TiO_2/Cu_2O-1 samples decrease to 2.76 ns and 2.62 ns, respectively. FTIR analysis shows that the formation of Cu_2O/TiO_2 heterojunction enhances the hydrophilicity of the sample, providing more H^+ for CO_2 reduction to generate CO. The energy bands and density of states obtained from DFT calculations further illustrate the formation of Cu_2O/TiO_2 heterojunctions. Work function calculations and SPM characterization confirm that Cu_2O/TiO_2 heterojunctions have better electron transfer capabilities than TiO_2. Meanwhile, the free energy of Cu_2O/TiO_{2Ov} in the * CO_2 to * COOH step is 0.088 eV lower than that of TiO_2, indicating that the Cu_2O/TiO_2 heterojunction containing oxygen vacancies has better catalytic performance.

STAR★METHODS

Detailed methods are provided in the online version of this paper and include the following:

- KEY RESOURCES TABLE
- RESOURCE AVAILABILITY
  - Lead contact
  - Materials availability
  - Data and code availability
- METHOD DETAILS
  - Materials
  - Preparation of Cu_2O/TiO_2
  - Characterization of the catalyst
  - Electrochemical measurement
  - Photocatalytic performance
  - DFT calculation models and methods

SUPPLEMENTAL INFORMATION

Supplemental information can be found online at https://doi.org/10.1016/j.isci.2024.109578.

ACKNOWLEDGMENTS

This work was supported by the financial supports from National Natural Science Foundation of China (grant no. 12172210).

AUTHOR CONTRIBUTIONS

Conceptualization, H.Q. and B.Y.; writing the original draft, H. Q.; methodology, H.Q. and Y.L.; writing – review and editing, B.Y., W.L., and C.Z.; funding acquisition, R.Z..

DECLARATION OF INTERESTS

The authors declare no competing interests.

Received: December 14, 2023
Revised: January 25, 2024
Accepted: March 25, 2024
Published: March 26, 2024

REFERENCES

1. Gao, J., Xue, J., Jia, S., Shen, Q., Zhang, X., Jia, H., Liu, X., Li, Q., and Wu, Y. (2021). Self-Doping Surface Oxygen Vacancy-Induced Lattice Strains for Enhancing Visible Light-Driven Photocatalytic H_2 Evolution over Black TiO_2. ACS Appl. Mater. Interfaces *13*, 18758–18771. https://doi.org/10.1021/acsami.1c01101.
2. Belgamwar, R., Verma, R., Das, T., Chakraborty, S., Sarawade, P., and Polshettiwar, V. (2023). Defects Tune the Strong Metal–Support Interactions in Copper Supported on Defected Titanium Dioxide Catalysts for CO_2 Reduction. J. Am. Chem. Soc. *145*, 8634–8646. https://doi.org/10.1021/jacs.3c01336.
3. Wang, T., Chen, L., Chen, C., Huang, M., Huang, Y., Liu, S., and Li, B. (2022). Engineering Catalytic Interfaces in $Cu^{\delta+}$/CeO_2-TiO_2 Photocatalysts for Synergistically Boosting CO_2 Reduction to Ethylene. ACS Nano *16*, 2306–2318. https://doi.org/10.1021/acsnano.1c08505.
4. Cheng, S.-P., Wei, L.-W., and Wang, H.-P. (2021). Photocatalytic Reduction of CO_2 to Methanol by Cu_2O/TiO_2 Heterojunctions. Sustainability *14*, 374. https://doi.org/10.3390/su14010374.
5. Yang, G., Qiu, P., Xiong, J., Zhu, X., and Cheng, G. (2022). Facilely anchoring Cu2O nanoparticles on mesoporous TiO2 nanorods for enhanced photocatalytic CO2 reduction through efficient charge transfer. Chin. Chem. Lett. *33*, 3709–3712. https://doi.org/10.1016/j.cclet.2021.10.047.
6. Qi, L., Wang, M., Xue, J., Zhang, Q., Chen, F., Liu, Q., Li, W., and Li, X. (2021). Simultaneous Tuning Band Gaps of Cu_2O and TiO_2 to Form S-Scheme Hetero-Photocatalyst. Chemistry A European J *27*, 14638–14644. https://doi.org/10.1002/chem.202102120.
7. Wang, M., Sun, L., Lin, Z., Cai, J., Xie, K., and Lin, C. (2013). p–n Heterojunction photoelectrodes composed of Cu_2O-loaded TiO_2 nanotube arrays with enhanced photoelectrochemical and photoelectrocatalytic activities. Energy Environ. Sci. *6*, 1211. https://doi.org/10.1039/c3ee24162a.
8. Aguirre, M.E., Zhou, R., Eugene, A.J., Guzman, M.I., and Grela, M.A. (2017). Cu_2O/TiO_2 heterostructures for CO_2 reduction through a direct Z-scheme: Protecting Cu_2O from photocorrosion. Appl. Catal. B Environ. *217*, 485–493. https://doi.org/10.1016/j.apcatb.2017.05.058.
9. Yuan, B., Qian, H., Cao, L., Zhu, R., and Luan, W. (2023). Designed Synthesis of Cu_2O Quantum Dots/TiO_2 Nanotubes Heterostructure as a Photocatalyst for Converting CO_2 to CH_4. Adv. Eng. Mater. *25*, 2301062. https://doi.org/10.1002/adem.202301062.
10. Etim, U.J., Zhang, C., and Zhong, Z. (2021). Impacts of the Catalyst Structures on CO_2 Activation on Catalyst Surfaces. Nanomaterials *11*, 3265. https://doi.org/10.3390/nano11123265.
11. Liu, L.L., Zhu, D., Cao, L.L., and Stephan, D.W. (2017). N-Heterocyclic carbene stabilized parent sulfenyl, selenenyl, and tellurenyl cations (XH^+, X = S, Se, Te). Dalton Trans. *46*, 3095–3099. https://doi.org/10.1039/C7DT00186J.
12. Mohite, S.V., Kim, S., Lee, C., Bae, J., and Kim, Y. (2022). Z-scheme heterojunction photocatalyst: Deep eutectic solvents-assisted synthesis of Cu_2O nanocluster improved hydrogen production of TiO_2. J. Alloys Compd. *928*, 167168. https://doi.org/10.1016/j.jallcom.2022.167168.
13. Li, Y., Wu, Z., Liu, T., Song, Z., and Zhang, Y. (2021). Modulating Photon Harvesting Through Constructing Oxygen Vacancies-Rich 0D/2D Plasmonic Bi/Bismuth Oxybromide Upconversion Nanosheets Toward Improved Solar Photocatalysis. Sol. RRL *5*, 2100619. https://doi.org/10.1002/solr.202100619.
14. Xue, J., Shen, Q., Liang, W., Liu, X., and Xu, B. (2013). Controlled synthesis of coaxial core–shell TiO_2/Cu_2O heterostructures by electrochemical method and their photoelectrochemical properties. Mater. Lett. *92*, 239–242. https://doi.org/10.1016/j.matlet.2012.10.127.
15. Bai, X., Ma, L., Dai, Z., and Shi, H. (2018). Electrochemical synthesis of p-Cu_2O/n-TiO_2 heterojunction electrode with enhanced photoelectrocatalytic activity. Mater. Sci. Semicond. Process. *74*, 319–328. https://doi.org/10.1016/j.mssp.2017.10.049.
16. Wei, T., Zhu, Y.-N., An, X., Liu, L.-M., Cao, X., Liu, H., and Qu, J. (2019). Defect Modulation of Z-Scheme TiO_2/Cu_2O Photocatalysts for Durable Water Splitting. ACS Catal. *9*, 8346–8354. https://doi.org/10.1021/acscatal.9b01786.
17. Xu, H., Zhang, Y., Wang, Y., Zhang, L., Zhang, Z., Zhong, L., He, Z., Zheng, Y., and Shen, Y. (2023). Heterojunction material $BiYO_3$/g-C_3N_4 modified with cellulose nanofibers for photocatalytic degradation of tetracycline. Carbohydr. Polym. *312*, 120829. https://doi.org/10.1016/j.carbpol.2023.120829.
18. Liu, G., Hou, G., Mao, X., Qi, X., Song, Y., Ma, X., Wu, J., Luo, G., Yao, H., and Liu, Q. (2022). Rational design of CeO_2/$Bi_7O_9I_3$ flower-like nanosphere with Z-scheme heterojunction and oxygen vacancy for enhancing photocatalytic activity. Chem. Eng. J. *431*, 133254. https://doi.org/10.1016/j.cej.2021.133254.
19. Li, J., Zhang, M., Guan, Z., Li, Q., He, C., and Yang, J. (2017). Synergistic effect of surface and bulk single-electron-trapped oxygen vacancy of TiO_2 in the photocatalytic reduction of CO_2. Appl. Catal. B Environ. *206*, 300–307. https://doi.org/10.1016/j.apcatb.2017.01.025.
20. Chen, X., Peng, X., Jiang, L., Yuan, X., Fei, J., and Zhang, W. (2022). Photocatalytic removal of antibiotics by MOF-derived Ti^{3+}- and oxygen vacancy-doped anatase/rutile TiO_2 distributed in a carbon matrix. Chem. Eng. J. *427*, 130945. https://doi.org/10.1016/j.cej.2021.130945.
21. Adamu, H., McCue, A.J., Taylor, R.S., Manyar, H.G., and Anderson, J.A. (2019). Influence of pretreatment on surface interaction between Cu and anatase-TiO_2 in the simultaneous photoremediation of nitrate and oxalic acid. J. Environ. Chem. Eng. *7*, 103029. https://doi.org/10.1016/j.jece.2019.103029.
22. Tahir, D., and Tougaard, S. (2012). Electronic and optical properties of Cu, CuO and Cu_2O studied by electron spectroscopy. J. Phys. Condens. Matter *24*, 175002. https://doi.org/10.1088/0953-8984/24/17/175002.
23. Stella, C., Prabhakar, D., Prabhu, M., Soundararajan, N., and Ramachandran, K. (2016). Oxygen vacancies induced room temperature ferromagnetism and gas sensing properties of Co-doped TiO_2 nanoparticles. J. Mater. Sci. Mater. Electron. *27*, 1636–1644. https://doi.org/10.1007/s10854-015-3935-x.
24. Zhou, S., Liu, Y., Li, J., Wang, Y., Jiang, G., Zhao, Z., Wang, D., Duan, A., Liu, J., and Wei, Y. (2014). Facile in situ synthesis of graphitic carbon nitride (g-C_3N_4)-N-TiO_2 heterojunction as an efficient photocatalyst

for the selective photoreduction of CO_2 to CO. Appl. Catal. B Environ. *158–159*, 20–29. https://doi.org/10.1016/j.apcatb.2014.03.037.

25. Jiao, J., Wei, Y., Zhao, Z., Liu, J., Li, J., Duan, A., and Jiang, G. (2014). Photocatalysts of 3D Ordered Macroporous TiO_2 -Supported CeO_2 Nanolayers: Design, Preparation, and Their Catalytic Performances for the Reduction of CO_2 with H_2O under Simulated Solar Irradiation. Ind. Eng. Chem. Res. *53*, 17345–17354. https://doi.org/10.1021/ie503333b.
26. Bika, P., Papailias, I., Giannakopoulou, T., Tampaxis, C., Steriotis, T.A., Trapalis, C., and Dallas, P. (2023). Prominent COF, g-C_3N_4, and Their Heterojunction Materials for Selective Photocatalytic CO_2 Reduction. Catalysts *13*, 1331. https://doi.org/10.3390/catal13101331.
27. Xu, J., Liu, X., Li, R., Shen, B., Zhou, Z., Deng, L., Liu, L., and Zhu, X. (2023). Production of renewable fuel from CO_2 by Co_3O_4/Cr doped MgAl-LDH p-n heterojunction catalyst. Fuel Process. Technol. *246*, 107762. https://doi.org/10.1016/j.fuproc.2023.107762.
28. Dong, W.-W., Jia, J., Wang, Y., An, J.-R., Yang, O.-Y., Gao, X.-J., Liu, Y.-L., Zhao, J., and Li, D.-S. (2022). Visible-light-driven solvent-free photocatalytic CO_2 reduction to CO by Co-MOF/Cu_2O heterojunction with superior selectivity. Chem. Eng. J. *438*, 135622. https://doi.org/10.1016/j.cej.2022.135622.
29. Zhao, X., Sun, L., Jin, X., Xu, M., Yin, S., Li, J., Li, X., Shen, D., Yan, Y., and Huo, P. (2021). Cu media constructed Z-scheme heterojunction of UiO-66-NH_2/Cu_2O/Cu for enhanced photocatalytic induction of CO_2. Appl. Surf. Sci. *545*, 148967. https://doi.org/10.1016/j.apsusc.2021.148967.
30. Jin, X., Cao, J., Wang, H., Lv, C., Xie, H., Su, F., Li, X., Sun, R., Shi, S., Dang, M., and Ye, L. (2022). Realizing improved CO_2 photoreduction in Z-scheme $Bi_4O_5Br_2$/AgBr heterostructure. Appl. Surf. Sci. *598*, 153758. https://doi.org/10.1016/j.apsusc.2022.153758.
31. Yang, C., Tan, Q., Li, Q., Zhou, J., Fan, J., Li, B., Sun, J., and Lv, K. (2020). 2D/2D Ti_3C_2 MXene/g-C_3N_4 nanosheets heterojunction for high efficient CO_2 reduction photocatalyst: Dual effects of urea. Appl. Catal. B Environ. *268*, 118738. https://doi.org/10.1016/j.apcatb.2020.118738.
32. Li, D., Zhu, B., Sun, Z., Liu, Q., Wang, L., and Tang, H. (2021). Construction of UiO-66/$Bi_4O_5Br_2$ Type-II Heterojunction to Boost Charge Transfer for Promoting Photocatalytic CO_2 Reduction Performance. Front. Chem. *9*, 804204. https://doi.org/10.3389/fchem.2021.804204.
33. Tang, J.y., Guo, R.t., Zhou, W.g., Huang, C.y., and Pan, W.g. (2018). Ball-flower like NiO/g-C_3N_4 heterojunction for efficient visible light photocatalytic CO_2 reduction. Appl. Catal. B Environ. *237*, 802–810. https://doi.org/10.1016/j.apcatb.2018.06.042.
34. Hong, L.f., Guo, R.t., Yuan, Y., Ji, X.y., Lin, Z.d., Yin, X.f., and Pan, W.g. (2022). 2D Ti_3C_2 decorated Z-scheme $BiOIO_3$/g-C_3N_4 heterojunction for the enhanced photocatalytic CO_2 reduction activity under visible light. Colloids Surf. A Physicochem. Eng. Asp. *639*, 128358. https://doi.org/10.1016/j.colsurfa.2022.128358.
35. Xiong, J., Zhang, M., Lu, M., Zhao, K., Han, C., Cheng, G., and Wen, Z. (2022). Achieving simultaneous Cu particles anchoring in mesoporous TiO_2 nanofabrication for enhancing photo-catalytic CO_2 reduction through rapid charge separation. Chin. Chem. Lett. *33*, 1313–1316. https://doi.org/10.1016/j.cclet.2021.07.052.
36. Lu, C., Li, X., Wu, Q., Li, J., Wen, L., Dai, Y., Huang, B., Li, B., and Lou, Z. (2021). Constructing Surface Plasmon Resonance on Bi_2WO_6 to Boost High-Selective CO_2 Reduction for Methane. ACS Nano *15*, 3529–3539. https://doi.org/10.1021/acsnano.1c00452.
37. Zou, Y., Yang, K., Chen, Q., Wang, H., and Meng, X. (2018). Molten salt construction of stable oxygen vacancies on TiO_2 for enhancement of visible light photocatalytic activity. RSC Adv. *8*, 36819–36825. https://doi.org/10.1039/C8RA07543C.
38. Luo, L., Zhang, T., Zhang, X., Yun, R., Lin, Y., Zhang, B., and Xiang, X. (2020). Enhanced Hydrogen Production from Ethanol Photoreforming by Site-Specific Deposition of Au on Cu_2O/TiO_2 p-n Junction. Catalysts *10*, 539. https://doi.org/10.3390/catal10050539.
39. Falah, M., MacKenzie, K.J.D., Knibbe, R., Page, S.J., and Hanna, J.V. (2016). New composites of nanoparticle Cu (I) oxide and titania in a novel inorganic polymer (geopolymer) matrix for destruction of dyes and hazardous organic pollutants. J. Hazard Mater. *318*, 772–782. https://doi.org/10.1016/j.jhazmat.2016.06.016.
40. Shao, Y.Y., Yuan, J.H., Li, X.N., Li, Z.M., Hu, Y.L., Cheng, Z.L., Liu, R.W., Zheng, R., Hou, Y.D., Li, M., et al. (2023). Compositional dependence of high temperature oxidation resistance in the L12-strengthened high-thermostability copper alloys. Corrosion Sci. *220*, 111281. https://doi.org/10.1016/j.corsci.2023.111281.
41. Ozkan, D.M., Uzun, A., Caglayan, B.S., and Aksoylu, A.E. (2023). A DFT study on the role of oxygen vacancy on m-ZrO_2 (111) in adsorption and dissociation of CO_2. Surf. Sci. *736*, 122336. https://doi.org/10.1016/j.susc.2023.122336.

STAR★METHODS

KEY RESOURCES TABLE

REAGENT or RESOURCE	SOURCE	IDENTIFIER
Chemicals, peptides, and recombinant proteins		
copper acetate	Macklin	6064-93-1
tetrabutyl titanate	Macklin	5593-70-4
potassium ferricyanide	Macklin	13746-66-2
Ethanol	Macklin	64-17-5
sodium hydroxide	Aladdin	1310-73-2
ethylenediamine tetraacetic acid		
sodium citrate	Shanghai Chemical Reagent	6132-04-3
sodium sulfate	Shanghai Chemical Reagent	7757-82-6

RESOURCE AVAILABILITY

Lead contact

Further information and requests for resources should be directed to and will be fulfilled by the lead contact, Binxia Yuan (yuanbinxia100@163.com).

Materials availability

This study did not generate new materials.

Data and code availability

- Any additional information required to reanalyze the data reported in this paper is available from the lead contact upon request.
- Data Availability Statement: All data reported in this paper will be shared by the lead contact upon request.
- Code: This paper does not report original code.

METHOD DETAILS

Materials

All chemicals are used directly without further purification. Copper acetate ($Cu(CH_3COO)_2$, AR, 99.0%), titanium butoxide ($C_{16}H_{36}O_4Ti$, analytical reagent), potassium ferricyanide ($K_3[FeC_6N_6]$, AR, 99.5%), and ethanol (C_2H_5OH, 99.7%) are purchased from Macklin. Sodium hydroxide (NaOH, GR, 97%) is purchased from Aladdin. Ethylenediamine tetraacetic acid, sodium citrate, and sodium sulfate (Na_2SO_4, AR) are purchased from Shanghai Chemical Reagent.

Preparation of Cu_2O/TiO_2

In a typical program, a certain amount of copper acetate, ethylenediaminetetraacetic acid (EDTA), sodium citrate, and NaOH are added to 50 mL of distilled water, and 0.5 mL of tetrabutyl titanate is dropped into the suspension and stirred at room temperature for 30 min. Then, the mixed solution is transferred in a 100 mL stainless steel high-pressure vessel lined with polytetrafluorethylene and heated at 180°C for 4 h. Afterward, the solid products are collected by centrifugation, washed several times with ethanol and distilled water, and dried at 60°C for 12 h. The obtained samples are named in the form of "A-B", where "A" represents the composition of the sample, and "B" represents the millimolar amount of copper acetate used.

Characterization of the catalyst

Scanning with an X-ray diffractometer (Bruker D8 Advance) determines the sample's composition. The morphology is characterized by transmission electron microscopy (JEM2100). Thermo Scientific K-Alpha obtains X-ray photoelectron spectroscopy (XPS). The absorption spectrum of the sample is measured using the Shimadzu UV-3600 spectrophotometer. The content of the Cu element is obtained through the inductively coupled plasma (ICP) technology (PerkinElmer NexION 300X). The photoluminescence spectra (PL) and time-resolved photoluminescence spectra (TRPL) of the sample are measured using a fluorescence spectrometer (OmniFluo 900). Measure oxygen vacancies using an electron paramagnetic resonance spectrometer (ESR-5000). The functional groups contained in the sample are measured using a Fourier transform infrared spectrometer (IRTracer-100). The surface potential of the sample is obtained using a scanning probe electron microscope (SPM-9700HT).

Electrochemical measurement

The CHI760E electrochemical workstation measures the electrochemical properties of the sample. In a typical three-electrode system, Ag/AgCl electrode and Pt foil are used as reference electrode and counter electrode, respectively, and the sample is dried onto 1 × 1.5 cm^2 FTO conductive glass to form a film as the working electrode. A 2.5 M $K_3[FeC_6N_6]$ electrolyte solution is used for electrochemical impedance spectroscopy (EIS) measurements, and a 0.1 M Na_2SO_4 solution is used for the I-t curve. Use a 500W xenon lamp (CEL-S500-T5) with an AREF total reflection filter as the light source.

Photocatalytic performance

CO_2 photocatalytic reduction experiments are conducted using a photocatalytic system (MC-SPH2O-a) equipped with a 5°C circulating cooling water apparatus. The testing system employs a solid-liquid mode, where the photocatalyst (50 mg) is dispersed in deionized water (100 mL). The system is degassed and purged to −0.1 MPa, and then illuminated by a 300W xenon lamp (full spectrum). Gas chromatography (GC2014C) with argon gas as the carrier is utilized for the analysis and quantification of the generated CO gas through reduction.

DFT calculation models and methods

The DMol3 module in the Material Studio (MS) software based on density functional theory is used for the calculation. Choose Perdew Burke Ernzerhof (PBE) as the calculation method in the generalized gradient approximation. The geometric structure of anatase TiO_2 (space group 141 I41/AMD) is optimized, and its (101) crystal plane is cut out. The TiO_2 model is obtained by adding a 2 × 2 × 1 supercell and a vacuum degree of 20 Å (Figure S5A). Create oxygen vacancies on the TiO_2 model surface and add the Cu_2O model near the oxygen vacancies to obtain the Cu_2O/TiO_{2Ov} model (Figure S5B). Then, $*CO_2$ molecules, *COOH, and *CO are adsorbed on Ti atoms near oxygen vacancies in the Cu_2O/TiO_{2Ov} model to construct a catalytic reaction process model. Select the k-point grid of the Brillouin zone as 2 × 3 × 1. Perform complete relaxation on all atoms within the crystal cell, with a relaxation convergence accuracy of 1.0 × 10^{-6} Ha, maximum stress set to 0.002 Ha/Å, and maximum displacement not exceeding 0.05 Å. The optimized geometric structure model uses DMol3 to calculate properties, such as free energy, energy band, density of states, and work function.